Frontiers in Heat and Mass Transfer

Tech Science Press

https://doi.org/10.32604/fhmt.2026.077952

ARTICLE

Numerical Simulation of Heat Transfer through Porous Hollow Building Block

Marina Astanina, Igor Miroshnichenko*, Gennadii Shashkin and Mikhail Sheremet

Laboratory on Convective Heat and Mass Transfer, Tomsk State University, Tomsk, Russia

*Corresponding Author: Igor Miroshnichenko. Email: miroshnichenko@mail.tsu.ru

Received: 20 December 2025; Accepted: 05 February 2026; Published: 30 April 2026

ABSTRACT: This paper explores the thermal behavior of a composite building element consisting of two air cavities inside a porous layer under isothermal heating of the side walls. The system presents a model of a thermal protection element or building envelope where heat transfer occurs through combined conduction in the porous medium and natural convection in the air gaps. The mathematical formulation is based on the Navier-Stokes equations and the Darcy-Brinkman formulation for the porous structure. The natural convection problem has been solved using the ψ–ω–θ formulation in dimensionless form (ψ—stream function, ω—vorticity, θ—temperature). The main heat transfer characteristics have been found to be strongly influenced by the governing parameters: *Ra* (the Rayleigh number), *Da* (Darcy number), ε (material porosity), and l_x, l_y (the size of the air gaps). Key findings: increasing the Rayleigh number from 10^4 to 10^6 enhances the mean Nusselt number from approximately 0.9 to 3.7 with intensification of convective heat transfer. Variations in the Darcy number over two orders of magnitude (10^{-4} to 10^{-2}) result in a similar change in the mean Nusselt number. Increasing porosity from $\varepsilon = 0.1$ to $\varepsilon = 0.8$ reduces the Nusselt number by less than 6%. The analysis of air cavity geometry shows that enlarging cavity dimensions increases flow intensity but produces only a moderate enhancement in heat transfer. Practical implications: optimal thermal insulation is achieved with high-porosity foam concrete ($\varepsilon \geq 0.6$) combined with low permeability ($Da \leq 10^{-4}$) and minimal air cavity dimensions. In this case, convective circulation is suppressed, and heat transfer remains conduction dominated with minimum values of the mean Nusselt number. The proposed model provides a physically consistent description of thermal transport in hybrid porous/fluid configurations and can serve as a basis for optimizing the thermal design of energy-efficient insulation structures and passive cooling devices.

KEYWORDS: Hollow building block; conjugate heat transfer; thermal insulation; free convection; porous medium; Brinkman–extended Darcy model; air cavities

1 Introduction

Improving the thermal insulation properties of building systems is a key area of modern research in heat and mass transfer. Multilayer composite structures combining porous materials and air cavities are widely used in insulation technologies for walls. Such systems provide increased thermal resistance by reducing conductive heat transfer and suppressing convective movement in air cavities. However, overall thermal performance significantly depends on the internal configuration, thermophysical properties, and geometric arrangement of components. Predicting and understanding the behavior of such systems is a key goal for numerical and experimental studies [1–5].

Problems in the simulation of such systems can be explained by the interplay of multiple physical mechanisms: conduction through the solid skeleton coupled with convection through a liquid phase and radiation at high temperatures [6–8]. The presence of additional air inserts in the porous structure complicates the

mathematical description [9–11]. Hollow foam concrete blocks are widely used in several construction applications. First, they are used in wall systems where horizontal orientation creates continuous air channels to improve thermal insulation. Second, these blocks are standard in floor and ceiling insulation. Third, they are utilized in non-load bearing partition walls for residential and industrial buildings. The present study employs a two-dimensional analysis. This approach investigates heat transfer in cross sectional planes perpendicular to the longitudinal axis of the blocks. Such an orientation represents the primary direction of heat flux through the building envelope. This methodological approach is well established in the literature. It has been successfully applied in previous studies of insulation systems [12–17].

The available literature contains some data on the impact of governing parameters on thermal and fluid flow behavior inside closed 2D cavities. For example, the Rayleigh number (Ra) is the ratio of buoyancy forces to dissipative forces. Buoyancy forces drive natural convection in a system. Viscosity and diffusion forces suppress this movement. Hulle et al. [1] have investigated heat transfer and fluid flow near a porous cylinder in an L-shaped enclosure using the lattice Boltzmann method ($10^3 \leq Ra \leq 10^6, 10^{-6} \leq Da \leq 10^{-2}$). The results have shown that an increase in Ra significantly improves heat transfer. The optimal location of the cylinder is in the lower part of the center. Doubling the cylinder width allows to increase in the mean Nusselt number by 46.5% at $Da = 10^{-6}$ with an enhancement in 118%. Yang et al. [8] have examined radiative and convective heat transfer in a closed volume with different temperatures on opposite walls. This analysis has revealed that increasing Ra intensifies natural convection and creates significant temperature gradients. Jalili et al. [2] have confirmed that increasing Ra results in a consistent improvement in heat transfer performance.

The Darcy number (Da) is responsible for the effective permeability (k) of the porous domain to a liquid and significantly affects the flow resistance and convection intensity. An analysis of thermogravitational convection in a vertical composite cylindrical enclosure has been presented by Ajibade et al. [3]. It has been shown that increasing the Brinkman number enhances temperature and velocity profiles. Higher Biot numbers reduce buoyancy force and fluid velocity. Khanafer and Vafai [18] have compared Darcy and Darcy-Forchheimer models. It has been demonstrated that cold cylinder presence enhances heat transfer by up to 76.1% at $Ra = 10^4$. Alam and Madanan [19] have experimentally explored Darcy, Forchheimer, and asymptotic flow regimes. They have found a transition value when the relationship between thermal and hydrodynamic boundary layer developments to grain size falls below 0.105 and a unified correlation for all regimes with ±11% deviations.

Moreover, the geometric configuration of the considered cavity has a strong effect on the natural convection patterns. Patrulescu et al. [4] have studied natural convection within an inclined square cavity saturated with a bidisperse porous material. It has been shown that the maximum average Nusselt number is observed for an inclination angle of $\pi/8$ (22.5°). The entropy release increases with increasing angle of inclination and is concentrated near the walls of the cavity. Paing and Anderson [20] have found that reducing the aspect ratio and reducing the roof inclination angle lower the convective heat transfer coefficient to 25% and 15% of its reference value, respectively. Nada and Said [21] have demonstrated that lateral rectangular ribs outperform annular ones by about 20% due to the appearance of numerous convection cells and thinner thermal boundary layers. Zhou et al. [22] have developed a novel 3D stochastic geometric model for carbon fibrous media, with the curved fiber model reducing computational error from 14.5% to 9%. Volschenk et al. [23] have advanced multilayer insulation modeling by introducing modifications based on the Knudsen number. Such a system successfully replicates characteristic S-curves across the entire vacuum pressure range. Ullah et al. [24] have studied natural convection heat transfer in a square cavity. The cavity models an electronic cabinet with solid walls and heated fins. The results help optimize thermal management in electronics.

The study of multilayered and composite systems has additional difficulties. For instance, Rahman et al. [5] have simulated transient free convection in a glass bead porous medium based on the LTNE formulation of the energy equation. The results have demonstrated that increasing bead diameter from 0.01 to 1.0 reduces the Nusselt numbers by 48.8% and 26%, respectively. Increasing sinusoidal temperature boundary wave frequency and amplitude dramatically enhances the heat transfer by 280.61% and 629.71%. Jia et al. [25] have studied composite systems combining nano-SiO_2-modified high porosity foam concrete and ultra-low conductivity panels with a vacuum-insulated core. The results have presented that the sandwich structure with a VIP core between two foam concrete layers exhibits superior performance with slower temperature change rates and lower total heat flux.

Numerical methods are one of the main methods for analyzing transport phenomena involving temperature and chemical potential gradients in porous structures. Xuan et al. [26] have determined the critical pore sizes for transition to turbulent flow regimes via the lattice Boltzmann framework. This study has concluded that the heating direction plays a decisive role: lateral heating yields the smallest critical pore size, and bottom heating yielded larger values. Top heating almost completely suppresses convection. Mirzai et al. [27] have used the finite element method to study entropy generation in a trapezoidal porous space. It should be noted that experimental verification in numerical studies remains a necessary procedure to ensure the accuracy of the model. Ngninjio et al. [11] have combined laboratory experiments on high-temperature borehole heat exchangers with OpenGeoSys modeling. They have shown that convection becomes noticeable at temperatures above 50°C; increasing charging efficiency by up to 35% but reducing heat recovery by 30%–35% due to thermal stratification. Ataei-Dadavi et al. [28] have identified two different heat transfer regimes depending on the relative scale of the thermal penetration depth to the particle size. Taghavi et al. [29] have demonstrated critical Rayleigh numbers for small liquid hydrogen tanks due to extreme temperature gradients using a bifurcation analysis of natural convection in spherical cryogenic insulation.

Understanding natural convection processes directly affects the development of energy storage systems and building isolation applications. For example, Ma et al. [10] have optimized thermochemical energy storage reactors using Co_3O_4/CoO redox systems. It has been found that a high value of porosity ($\approx$ 0.9) facilitates rapid the reaction produced oxygen while generating thermal power peaks of 61.95 W. At the same time, the increased inlet temperature reduces the reaction time by 90%. Veit et al. [30] have investigated the thermal performance of loose wood fiber insulation. The authors have reported that internal convection increases effective U-values by up to 90% under steady-state conditions. However, this effect is less pronounced under dynamic conditions. Angelotti et al. [31] have characterized recycled cotton fiber with a thermal conductivity in the range of 0.0381 to 0.0546 W/(m·K). They have presented temperature and relative humidity as the most influential parameters.

Extensive research has been conducted in this field. However, significant knowledge gaps still exist. Investigations into systems with multiple air cavities are particularly limited [1–5,8,18]. Specifically, the interaction between cavities is not well understood. Research on optimal cavity arrangements remains insufficient. Transient behavior under realistic boundary conditions needs a comprehensive understanding [5,11]. Three-dimensional effects require systematic investigation beyond 2D simplifications [1,2,27]. Turbulence modeling using advanced techniques like LES or DNS would provide deeper insights [32,33]. Coupled phenomena addressing convection with radiation, moisture transport, and phase change need attention [8,27,31]. Optimization frameworks considering multiple objectives require development [1–4,10,18]. In addition, experimental validation combining optical methods with thermal measurements in multi-cavity configurations can be an essential part of research [11,28].

This study focuses on simulating the coupled heat transfer mechanisms (conduction in a porous matrix and natural convection in air cavities) induced by isothermal heating of the lateral walls of a composite enclosure. The specific objectives are to: develop and validate a numerical model coupling Navier-Stokes equations in fluid regions with the Brinkman-extended Darcy model in porous regions; systematically investigate the effects of Ra (10^4–10^6), Da (10^{-4}–10^{-2}), ε (0.1–0.8) and cavity dimensions (l_x, l_y) on thermal performance; identify optimal parameter ranges that minimize convective heat transfer and maximize thermal insulation; provide quantitative design guidelines for energy efficient hollow building blocks. The results will fill gaps in existing knowledge and provide detailed information on the interaction of convective flows within individual cavities, the influence of cavity size, and the impact of thermophysical properties on the thermal behavior of insulation and cooling devices. Despite extensive research on natural convection in porous media and in air cavities separately, the coupled thermal behavior of dual air cavities embedded within a porous matrix remains largely unexplored. This configuration is highly relevant for hollow building blocks. In such elements, convective flows within multiple cavities interact with heat conduction through the porous skeleton. This interaction determines the overall thermal performance.

2 Model Description and Governing Equations

Fig. 1 illustrates the schematic of the physical model: a closed enclosure containing a porous layer with two internal air cavities under isothermal heating and cooling of the side walls. The work analyzes buoyancy-driven flow and heat transfer in a fluid saturated porous enclosure. Convection is generated by maintaining opposing vertical walls at different constant temperatures. The cavity consists of a Newtonian fluid with variable thermophysical properties and a permeable isotropic porous medium located near the heated boundary of the cavity. The following standard assumptions are made: (1) no turbulence model is employed; the flow is treated as laminar; (2) the Boussinesq approximation holds for the buoyancy term; (3) the horizontal boundaries (top and bottom) are considered adiabatic.

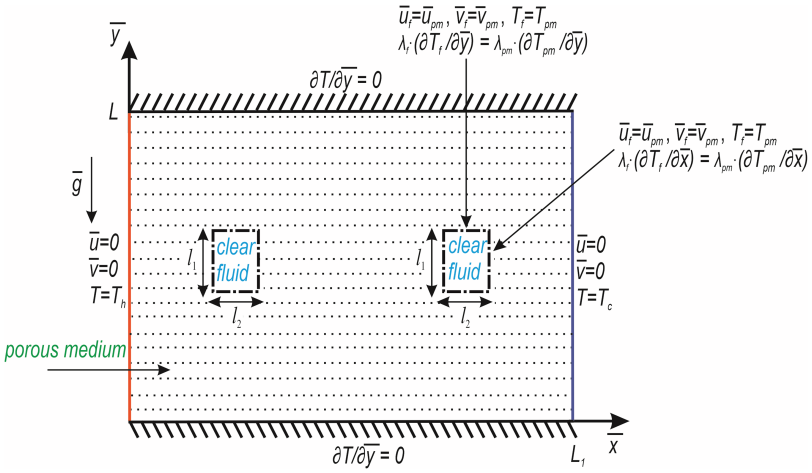

Figure 1: Considered insulation system.

The present analysis consists of several fundamental assumptions, including the fluid properties and flow characteristics. All boundaries of the enclosure are impermeable. A local thermal equilibrium (LTE) condition is assumed for the homogeneous and isotropic porous structure. The transient Darcy-Brinkman model [34,35] governs momentum transfer in the porous region. The domain contains two identical

air cavities symmetrically arranged about the vertical axis (y-axis). The thermophysical properties of all materials are given in Table 1.

Table 1: Material properties used in the simulation.

Characteristic	ρ [kg/m^3]	c [J/(kg·K)]	λ [W/(m·K)]
Fluid (air)	1.2754	1005	0.022
Porous medium (foam concrete)	500	1000	0.13

The model is based on the 2D conservation equations for mass, momentum and energy [36]:

- for the air cavities:

$$\frac{\partial \overline{u}}{\partial \bar{x}} + \frac{\partial \overline{v}}{\partial \overline{y}} = 0, \tag{1}$$

$$\rho\left(\frac{\partial \overline{u}}{\partial t} + \overline{u}\frac{\partial \overline{u}}{\partial \bar{x}} + \overline{v}\frac{\partial \overline{u}}{\partial \overline{y}}\right) = -\frac{\partial p}{\partial \bar{x}} + \overline{\mu}\left(\frac{\partial^2 \overline{u}}{\partial \bar{x}^2} + \frac{\partial^2 \overline{u}}{\partial \overline{y}^2}\right), \tag{2}$$

$$\rho\left(\frac{\partial \overline{v}}{\partial t} + \overline{u}\frac{\partial \overline{v}}{\partial \bar{x}} + \overline{v}\frac{\partial \overline{v}}{\partial \overline{y}}\right) = -\frac{\partial p}{\partial \overline{y}} + \overline{\mu}\left(\frac{\partial^2 \overline{v}}{\partial \bar{x}^2} + \frac{\partial^2 \overline{v}}{\partial \overline{y}^2}\right) + \rho g\beta\left(T - T_c\right), \tag{3}$$

$$\frac{\partial T}{\partial t} + \overline{u}\frac{\partial T}{\partial \bar{x}} + \overline{v}\frac{\partial T}{\partial \overline{y}} = \frac{\lambda_f}{(\rho c)_f}\left(\frac{\partial^2 T}{\partial \bar{x}^2} + \frac{\partial^2 T}{\partial \overline{y}^2}\right), \tag{4}$$

- for the porous part of the enclosure [35,36]:

$$\frac{\partial \overline{u}}{\partial \bar{x}} + \frac{\partial \overline{v}}{\partial \overline{y}} = 0, \tag{5}$$

$$\rho\left(\frac{1}{\varepsilon}\frac{\partial \overline{u}}{\partial t} + \frac{\overline{u}}{\varepsilon^2}\frac{\partial \overline{u}}{\partial \bar{x}} + \frac{\overline{v}}{\varepsilon^2}\frac{\partial \overline{u}}{\partial \overline{y}}\right) = -\frac{\partial p}{\partial \bar{x}} + \frac{\overline{\mu}}{\varepsilon}\left(\frac{\partial^2 \overline{u}}{\partial \bar{x}^2} + \frac{\partial \overline{u}^2}{\partial \overline{y}^2}\right) - \frac{\overline{\mu}}{K}\overline{u}, \tag{6}$$

$$\rho\left(\frac{1}{\varepsilon}\frac{\partial \overline{v}}{\partial t} + \frac{\overline{u}}{\varepsilon^2}\frac{\partial \overline{v}}{\partial \bar{x}} + \frac{\overline{v}}{\varepsilon^2}\frac{\partial \overline{v}}{\partial \overline{y}}\right) = -\frac{\partial p}{\partial \overline{y}} + \frac{\overline{\mu}}{\varepsilon}\left(\frac{\partial^2 \overline{v}}{\partial \bar{x}^2} + \frac{\partial^2 \overline{v}}{\partial \overline{y}^2}\right) - \frac{\overline{\mu}}{K}\overline{v} + \rho g\beta\left(T - T_c\right), \tag{7}$$

$$\eta\frac{\partial T}{\partial t} + \overline{u}\frac{\partial T}{\partial \bar{x}} + \overline{v}\frac{\partial T}{\partial \overline{y}} = \frac{\lambda_{pm}}{(\rho c)_f}\left(\frac{\partial^2 T}{\partial \bar{x}^2} + \frac{\partial^2 T}{\partial \overline{y}^2}\right). \tag{8}$$

The following notation has been used: $\bar{x}, \overline{y}$ are the Cartesian coordinates with corresponding velocity components $\overline{u}, \overline{v}$; the fluid density ρ; the time t; the pressure p; the temperature T; the dynamic viscosity for reference temperature μ_0; the permeability of the porous layer K; the standard gravity g; the volumetric thermal expansion coefficient β; the effective specific heat of the porous medium c; the porous medium's thermal conductivity $\lambda_{pm} = \varepsilon \cdot \lambda_f + (1-\varepsilon) \cdot \lambda_s$; the ratio of the effective volumetric heat capacity of the porous medium to that of the fluid $\eta = \varepsilon + (1-\varepsilon)\frac{(\rho c)_s}{(\rho c)_f}$.

The following transformation to $\overline{\psi}$ (stream function) and $\overline{\omega}$ (vorticity) variables is applied:

$$\left.\begin{aligned} \overline{u} &= \frac{\partial \overline{\psi}}{\partial \overline{y}} \\ \overline{v} &= -\frac{\partial \overline{\psi}}{\partial \bar{x}} \end{aligned}\right\} \Rightarrow \overline{\omega} = \frac{\partial \overline{v}}{\partial \bar{x}} - \frac{\partial \overline{u}}{\partial \overline{y}}. \tag{9}$$

The following parameters have been chosen as the scales of distance, time, velocity, temperature, stream function and vorticity:

$$L, \sqrt{g\beta\Delta T/L},\ \sqrt{g\beta\Delta TL},\ \Delta T = T_h - T_c, \sqrt{g\beta\Delta TL^3},\ \sqrt{L/g\beta\Delta T}$$

The new variables are introduced through the following relations [34,35]:

$$\begin{gathered} x = \bar{x}/L, u = \overline{u}/\sqrt{g\beta\Delta TL},\ y = \overline{y}/L, v = \overline{v}/\sqrt{g\beta\Delta TL},\ \theta = (T - T_c)/\Delta T. \\ \tau = t\sqrt{g\beta\Delta T/L},\ \omega = \overline{\omega}\sqrt{L/g\beta\Delta T},\ \ \psi = \overline{\psi}/\sqrt{g\beta\Delta TL^3} \end{gathered} \tag{10}$$

In terms of these dimensionless variables (ψ, ω, θ) the governing equations for mass, momentum and energy transform into the following coupled system:

- for the air cavities:

$$\frac{\partial^2\psi}{\partial x^2} + \frac{\partial^2\psi}{\partial y^2} = -\omega, \tag{11}$$

$$\frac{\partial\omega}{\partial\tau} + \frac{\partial\psi}{\partial y}\frac{\partial\omega}{\partial x} - \frac{\partial\psi}{\partial x}\frac{\partial\omega}{\partial y} = \sqrt{\frac{Pr}{Ra}}\left(\frac{\partial^2\omega}{\partial x^2} + \frac{\partial^2\omega}{\partial y^2}\right) + \frac{\partial\theta}{\partial x}, \tag{12}$$

$$\frac{\partial\theta}{\partial\tau} + \frac{\partial\psi}{\partial y}\frac{\partial\theta}{\partial x} - \frac{\partial\psi}{\partial x}\frac{\partial\theta}{\partial y} = \frac{1}{\sqrt{Pr\cdot Ra}}\left(\frac{\partial^2\theta}{\partial x^2} + \frac{\partial^2\theta}{\partial y^2}\right), \tag{13}$$

- for the porous part of the enclosure [35]:

$$\frac{\partial^2\psi}{\partial x^2} + \frac{\partial^2\psi}{\partial y^2} = -\omega, \tag{14}$$

$$\varepsilon\frac{\partial\omega}{\partial\tau} + \frac{\partial\psi}{\partial y}\frac{\partial\omega}{\partial x} - \frac{\partial\psi}{\partial x}\frac{\partial\omega}{\partial y} = \varepsilon\sqrt{\frac{Pr}{Ra}}\left(\frac{\partial^2\omega}{\partial x^2} + \frac{\partial^2\omega}{\partial y^2} - \varepsilon\frac{\omega}{Da}\right) + \varepsilon^2\frac{\partial\theta}{\partial x}, \tag{15}$$

$$\eta\frac{\partial\theta}{\partial\tau} + \frac{\partial\psi}{\partial y}\frac{\partial\theta}{\partial x} - \frac{\partial\psi}{\partial x}\frac{\partial\theta}{\partial y} = \frac{\alpha_{pm}/\alpha_f}{\sqrt{Pr\cdot Ra}}\left(\frac{\partial^2\theta}{\partial x^2} + \frac{\partial^2\theta}{\partial y^2}\right). \tag{16}$$

Here the Darcy number, the Prandtl number and Rayleigh number have a following form [34,35]:

$$Da = \frac{K}{L^2},\ \ Pr = \frac{\mu_0}{\rho\alpha},\ \ \ Ra = \frac{\rho g\beta\Delta TL^3}{\alpha\mu_0}. \tag{17}$$

The initial and boundary relations for mathematical model (11)–(16) have a following form:

$$\tau = 0: \quad \psi = \omega = \theta = 0 \text{ at } 0 \le x \le H = L/L_1,\ 0 \le y \le 1$$

$$\tau > 0: \quad \psi = 0,\ \omega = -\frac{\partial^2\psi}{\partial x^2},\ \theta_w = 1 \text{ at } x = 0,\ 0 \le y \le 1$$

$$\psi = 0,\ \omega = -\frac{\partial^2\psi}{\partial x^2},\ \theta_w = 0 \text{ at } x = H,\ 0 \le y \le 1$$

$$\psi = 0,\ \omega = -\frac{\partial^2\psi}{\partial y^2},\ \frac{\partial\theta}{\partial y} = 0 \text{ at } y = 0,\ 1,\ 0 < x < H$$

at horizontal internal porous-fluid interface:

$$\begin{cases} \psi_f = \psi_{pT} \\ \dfrac{\partial \psi_f}{\partial y} = \dfrac{\partial \psi_{pm}}{\partial y} \end{cases} \quad \begin{cases} \omega_f = \omega_{pm} \\ \dfrac{\partial \omega_f}{\partial y} = \dfrac{\partial \omega_{pm}}{\partial y} \end{cases} \quad \begin{cases} \theta_f = \theta_{pm} \\ \dfrac{\partial \theta_f}{\partial y} = \dfrac{\lambda_{pm}}{\lambda_f} \dfrac{\partial \theta_{pm}}{\partial y} \end{cases}$$

at vertical internal porous-fluid interface:

$$\begin{cases} \psi_f = \psi_{pm} \\ \dfrac{\partial \psi_f}{\partial x} = \dfrac{\partial \psi_{pm}}{\partial x} \end{cases} \quad \begin{cases} \omega_f = \omega_{pm} \\ \dfrac{\partial \omega_f}{\partial x} = \dfrac{\partial \omega_{pm}}{\partial x} \end{cases} \quad \begin{cases} \theta_f = \theta_{pm} \\ \dfrac{\partial \theta_f}{\partial x} = \dfrac{\lambda_{pm}}{\lambda_f} \dfrac{\partial \theta_{pm}}{\partial x} \end{cases} \tag{18}$$

The average Nusselt number at the isothermal hot wall is evaluated to quantify the convective heat transfer enhancement. It is defined as:

$$\overline{Nu} = -\int_0^1 \frac{\partial \theta}{\partial x} dy. \tag{19}$$

3 Solution Algorithms

The system of governing Eqs. (11)–(16) subject to the initial and boundary conditions (18) has been solved numerically using a finite-difference method (FDM) on a uniform grid. Spatial discretization of the convective and diffusive terms has been performed with second-order accurate central difference schemes. For the temporal integration of the parabolic equations, the Samarskii locally one-dimensional scheme has been employed. The resulting sets of tridiagonal linear equations at each fractional time step have been solved using the Thomas algorithm. The elliptic equations for the stream function (11) and (14) have been discretized via a standard five-point stencil based on central differences for the second derivatives [34,35]. The obtained system of linear algebraic equations has been solved iteratively using the successive over-relaxation method. The optimal value of the relaxation parameter has been determined through preliminary numerical experiments to ensure rapid convergence. The simulations have been performed using an in-house C++ solver.

A comprehensive validation analysis has been conducted using established benchmark cases from the literature [37]. Fig. 2 presents a qualitative validation of our numerical model by comparing it to the benchmark solution [37]. This work has analyzed buoyancy-driven flow in a partially porous enclosure with isothermal lateral heating.

The mesh independence of the solution has been verified by testing several grid configurations. Table 2 illustrates values of the maximum fluid flow inside the enclosure and average Nusselt number on the hot wall for different mesh sizes at $Pr = 0.7$, $Ra = 10^5$, $\varepsilon = 0.8$, $Da = 10^{-4}$, $l_x = 0.4$, $l_y = 0.2$, $\tau = 6000$. Based on this sensitivity analysis a grid of 400 × 200 control elements has been chosen for next computations.

The relative error of the values has been determined by the following relationship:

$$\Delta\chi = \frac{\left|\chi_{i\times j} - \chi_{600\times 300}\right|}{\chi_{i\times j}} \times 100\%$$

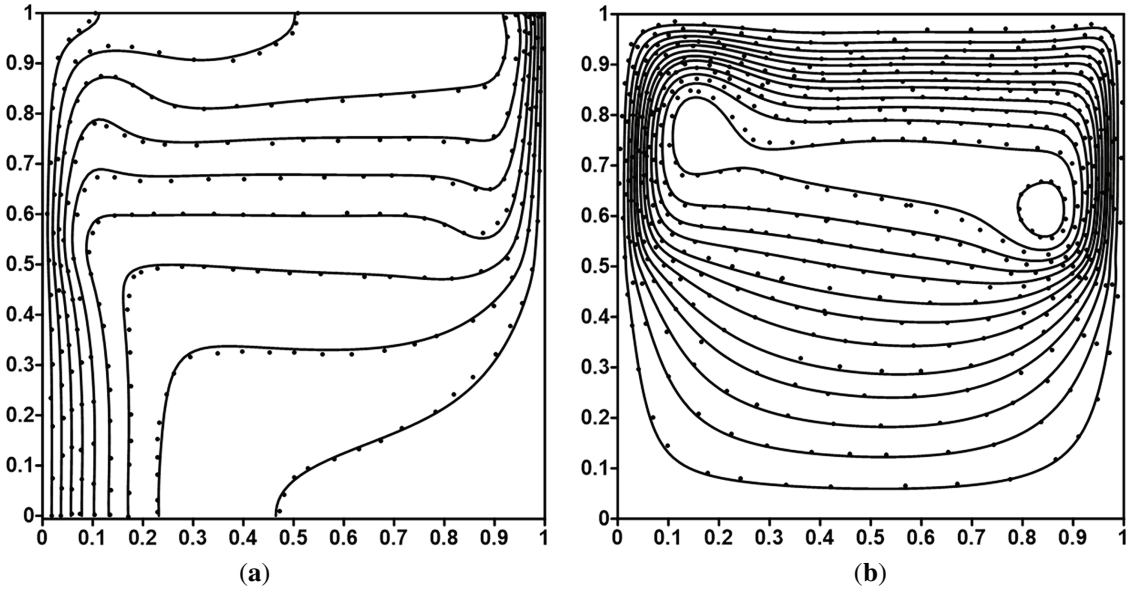

Figure 2: Comparison with the test problem at $Ra = 10^6$, $Da = 10^{-5}$: solid lines (obtained data), dashed lines (data of [37]), (**a**) isolines of the temperature, (**b**) isolines of the stream function.

Table 2: Values of the integral parameters for different mesh sizes.

	$\overline{Nu}$	$\lvert\psi\rvert_{max}$	$\Delta_{\overline{Nu}}$	$\Delta_{\lvert\psi\rvert_{max}}$	Calculation Time
50 × 25	0.97043	0.0157237	8.44%	12.55%	≈7 h
100 × 50	0.912592	0.0145186	2.64%	5.29%	≈8 h
200 × 100	0.895566	0.0139678	0.79%	1.56%	≈15 h
300 × 150	0.891371	0.0138359	0.32%	0.62%	≈28 h
400 × 200	0.889734	0.0137861	0.14%	0.26%	≈34 h
600 × 300	0.888497	0.0137492	–	–	≈96 h

The time step independence of the solution has been verified by testing several values of $\Delta\tau$. Table 3 shows the values of the maximum intensity of the flow circulation inside the enclosure and average Nusselt number on the hot wall for different time steps at $Pr = 0.7$, $Ra = 10^5$, $\varepsilon = 0.8$, $Da = 10^{-4}$, $l_x = l_2/L_1 = 0.4$, $l_y = l_1/L = 0.2$, $\tau = 6000$, 400 × 200 points. Based on this comparison a time step $\Delta\tau = 0.001$ has been chosen for next computations.

The relative error of the values has been determined by the following relationship:

$$\Delta\chi_{\Delta\tau_i} = \frac{\left|\chi_{\Delta\tau_i} - \chi_{\Delta\tau=0.0005}\right|}{\chi_{\Delta\tau_i}} \times 100\%$$

Table 3: Values of the integral parameters for different time steps.

	$\overline{Nu}$	$\lvert\psi\rvert_{\max}$	$\Delta_{\overline{Nu}}$	$\Delta_{\lvert\psi\rvert_{max}}$	Calculation Time
$\Delta\tau = 0.0005$	0.889677	0.0137847	–	–	≈96 h
$\Delta\tau = 0.001$	0.889734	0.0137861	0.006%	0.01%	≈34 h
$\Delta\tau = 0.002$	0.889843	0.0137889	0.018%	0.03%	≈9 h
$\Delta\tau = 0.01$	0.890614	0.0138097	0.1%	0.18%	≈6 h
$\Delta\tau = 0.1$	–	–	–	–	–

4 Numerical Results and Analysis

The following set of governing parameter values has been adopted in the numerical simulations: $Pr = 0.7$ (Prandtl number), $Ra = 10^4$–10^6 (Rayleigh number), $\varepsilon = 0.1$–0.8 (porosity of the porous structure), $Da = 10^{-4}$–10^{-2} (Darcy number), $l_x = 0.4$–0.8 (dimensionless size of the clear part in x-direction), $l_y = 0.2$–0.4 (dimensionless length of the clear part in y-direction), $\tau = 0$–6000 (dimensionless time). The influence of these parameters on the flow structure and heat transfer is shown in Figs. 3–8.

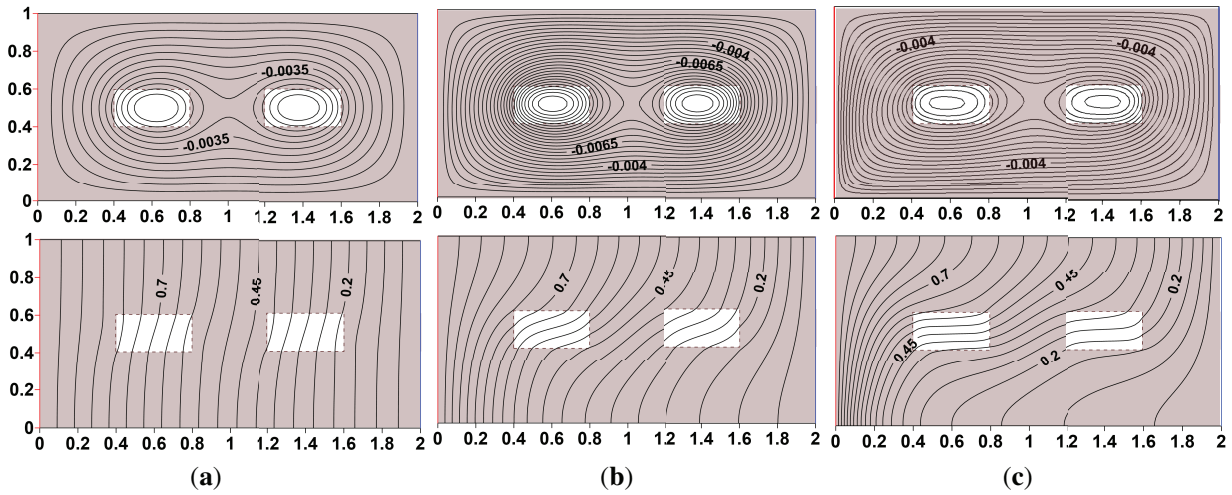

Figure 3: Streamlines and temperature contours at $Da = 10^{-4}$, $\varepsilon = 0.8$, $Da = 10^{-4}$, $l_x = 0.4$, $l_y = 0.2$, (**a**) $Ra = 10^4$, (**b**) $Ra = 10^5$, (**c**) $Ra = 10^6$.

Fig. 3 presents distributions of ψ and θ at $\varepsilon = 0.8$, $Da = 10^{-4}$, $l_x = 0.4$, $l_y = 0.2$, and for varying Ra. The obtained results show a strong dependence on the Ra. At $Ra = 10^4$ (Fig. 3a), the field distribution reflects a weak convective circulation. Two symmetrical vortices are formed inside the air cavities, with clockwise rotation in the left cavity and counterclockwise rotation in the right cavity. The temperature field shows predominantly conductive heat transfer with vertical isotherms in the porous matrix region and minimal distortion near the cavity boundaries. The observed difference in thermal conductivity between the foam concrete ($\lambda_s = 0.13$ W/(m·K)) and air ($\lambda_f = 0.022$ W/(m·K)) results in preferential heat conduction through the porous medium. At $\varepsilon = 0.8$, the effective thermal conductivity of the porous layer $\lambda_{pm} = \varepsilon \cdot \lambda_f + (1 - \varepsilon) \cdot \lambda_s \approx 0.044$ W/(m·K). The thermal conductivity of a porous material is twice that of air. This leads to increased heat transfer through the solid structure. This phenomenon occurs despite the limited convective movement.

As the Rayleigh number increases to $Ra = 10^5$ (Fig. 3b), the intensity of convective motion becomes more pronounced. The maximum absolute value of the stream function increases with stronger fluid circulation within the air gaps. The isotherms are noticeably curved, especially near the hot wall and inside the cavities. This indicates increased convective heat transfer. Thermal boundary layers near vertical walls become thinner (improving heat transfer efficiency). The temperature distribution inside the porous matrix remains uniform due to the higher effective thermal conductivity compared to air cavities. In air gaps, convective distortion of the isotherms is more noticeable. The contrast between heat transfer in the porous region and heat transfer in the air parts is becoming more obvious.

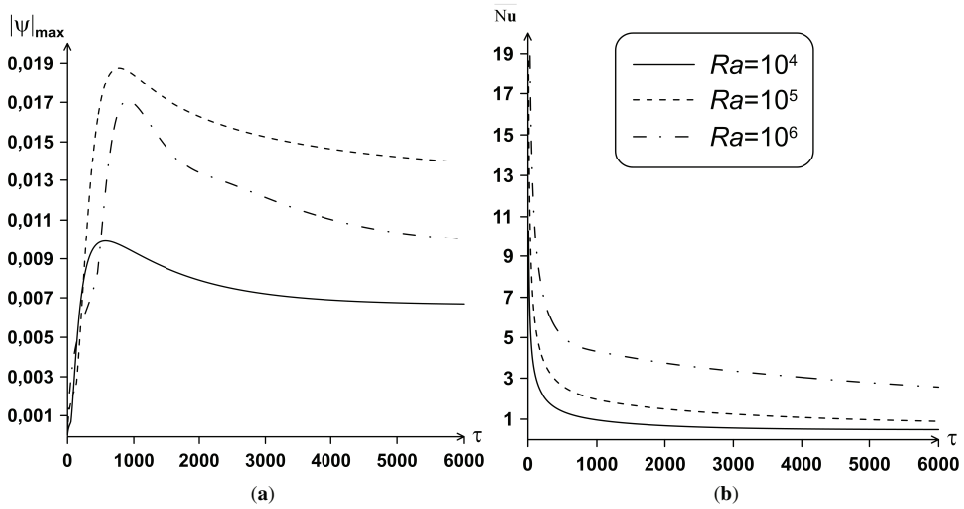

Figure 4: Variation of the integral parameters vs. *Ra* and τ, (**a**) maximum absolute value of the stream function, (**b**) the mean Nusselt number at the heated boundary.

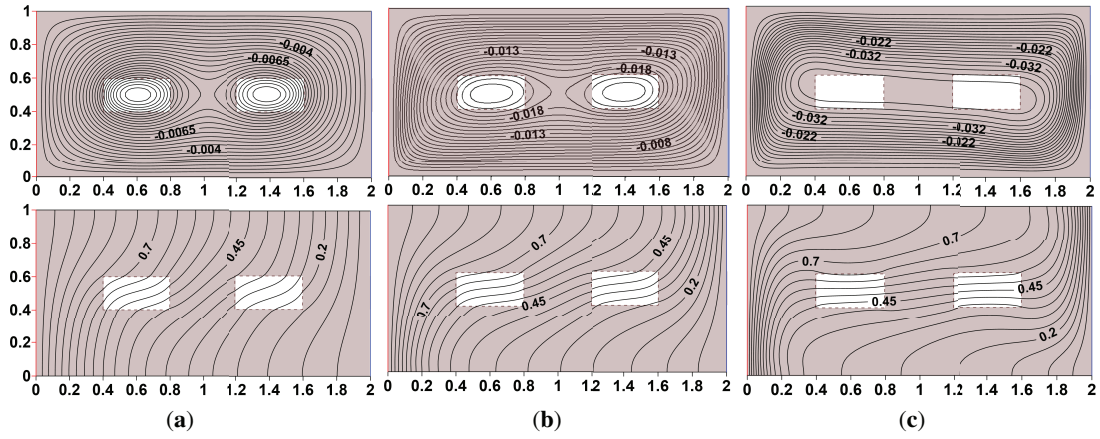

Figure 5: Streamlines and temperature contours at $Ra = 10^5$, $\varepsilon = 0.8$, $l_x = 0.4$, $l_y = 0.2$, (**a**) $Da = 10^{-4}$, (**b**) $Da = 10^{-3}$, (**c**) $Da = 10^{-2}$.

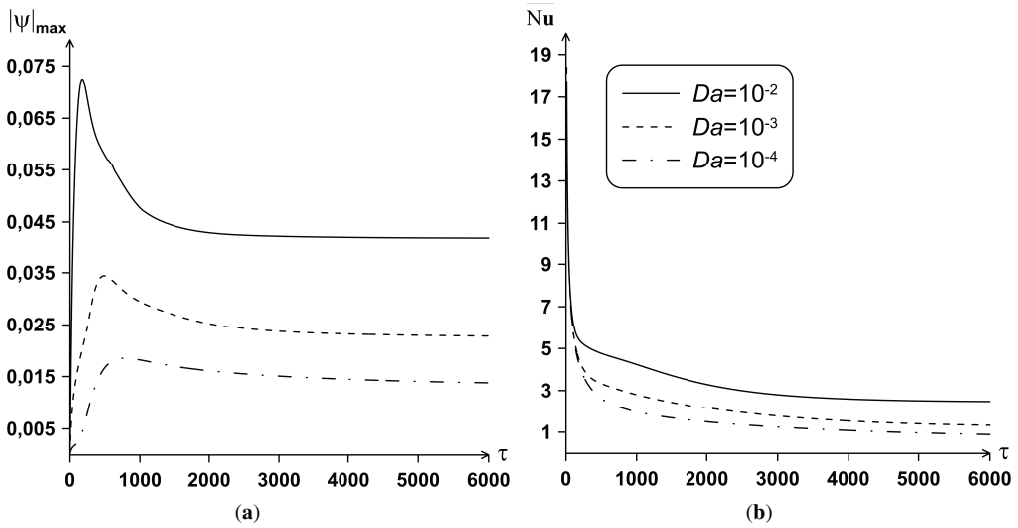

Figure 6: Variation of the integral parameters vs. *Da* and τ, (**a**) maximum absolute value of the stream function, (**b**) the mean Nusselt number at the heated boundary.

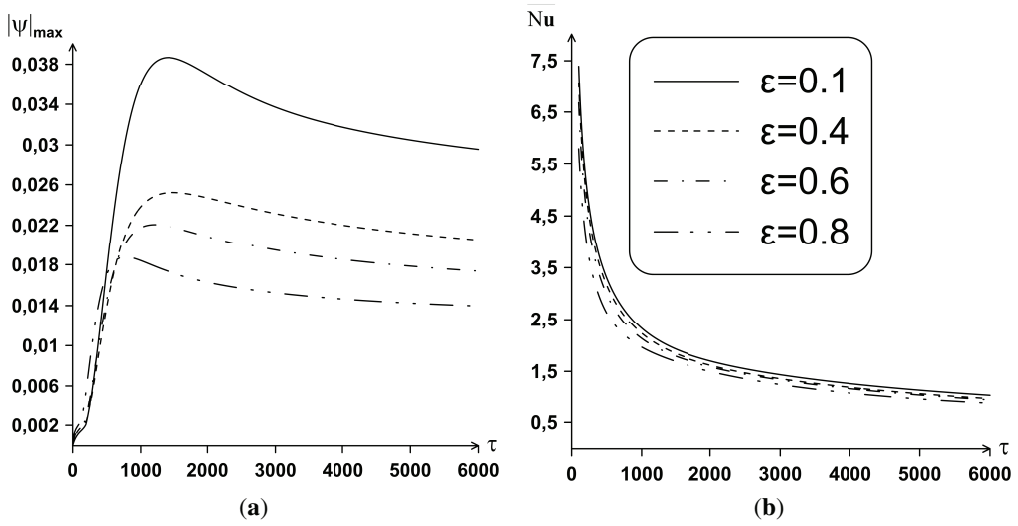

Figure 7: Variation of the integral parameters vs. the porosity ε and τ, (**a**) maximum absolute value of the stream function, (**b**) the mean Nusselt number at the heated boundary.

At $Ra = 10^6$ (Fig. 3c), the convective regime becomes dominant in the air cavities. The flow lines show a high intensity of circulation with the vortex cores shifting towards the central region of each cavity. The isotherms exhibit significant distortion across the entire domain. Thermal stratification is pronounced in the upper regions of the cavities. Heat flows along the heated wall and descending along the cooled wall are clearly visible. The porous medium effectively suppresses convection in the intermediate region as evidenced by the preservation of relatively undistorted isotherms inside the porous matrix. This behavior is explained by the high flow resistance due to the low permeability of foam concrete and increased thermal conductivity ($\alpha_{\text{pm}} = \lambda_{\text{pm}}/(\rho c)_{pm}$) compared to pure air ($\alpha_f = \lambda_f/(\rho c)_f$), which promotes thermal conductivity, transfer, and damping of convective vibrations.

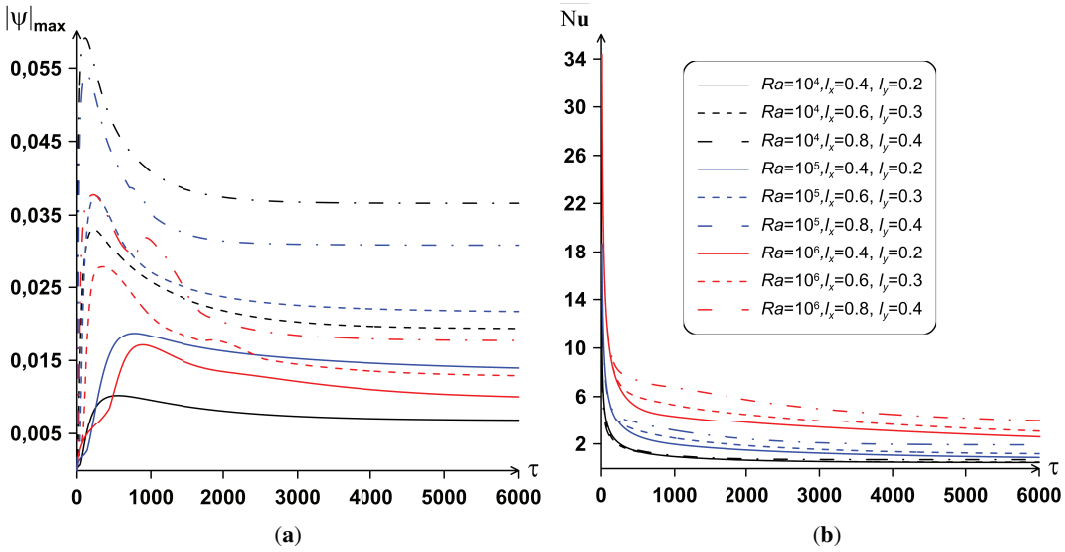

Figure 8: Variation of the integral parameters vs. the air cavities sizes and time, (**a**) maximum absolute value of the stream function, (**b**) the mean Nusselt number at the heated boundary.

Fig. 4 demonstrates the effects of the Rayleigh number on the integral parameters of the processes at $\varepsilon = 0.8$, $Da = 10^{-4}$, $l_x = 0.4$, $l_y = 0.2$. Fig. 4a depicts the variation of the maximum absolute value of the stream function ($|\psi|_{max}$) with dimensionless time for three different values of the Rayleigh number. At $Ra = 10^4$ the system reaches steady state quickly at $\tau \approx 2000$ with $|\psi|_{max} \approx 0.01$ (weak convective circulation). For $Ra = 10^5$ the transient phase extends longer and the steady-state value increases to approximately $|\psi|_{max} \approx 0.019$ (enhancement in the flow intensity). At this Rayleigh number, convective motion in air cavities becomes intense enough to compete with heat transfer due to conduction through the porous medium . At $Ra = 10^6$ $|\psi|_{max} \approx 0.017$ which represents a decrease compared to $Ra = 10^5$. This nonlinear growth of $|\psi|_{max}$ with Ra confirms the increasingly dominant role of buoyancy forces over viscous dissipation and thermal diffusion.

Fig. 4b illustrates the time-dependent average Nusselt number at the hot boundary of the cavity. For $Ra = 10^4$ the average Nusselt number stabilizes at approximately $\overline{Nu} \approx 0.9$. Heat transfer occurs primarily via conduction with a modest convective contribution. The low thermal conductivity of air ($\lambda_f = 0.022$ W/(m·K)) limits the efficiency of purely conductive transport while the porous foam concrete layer with $\lambda_{pm} \approx 0.044$ W/(m·K) provides a more effective conductive pathway in the intermediate region. At $Ra = 10^5$ the steady-state value increases to $\overline{Nu} \approx 1.2$ reflecting an enhancement in convective heat transfer. This increase demonstrates that convection within the air cavities significantly augments the overall heat transfer. For $Ra = 10^6$ the average Nusselt number reaches $\overline{Nu} \approx 3.0$ with an additional increase. The Nusselt number grows sublinearly with the Rayleigh number. This indicates high thermal resistance in the foam concrete layer. This resistance remains significant even at high Rayleigh numbers. The layer effectively limits the heat flux through the system. The curves exhibit a characteristic monotonic increase during the initial transition period. This is followed by an asymptotic approach to steady-state values. The time to reach quasi-steady conditions increases with the Rayleigh number. This reflects longer characteristic time scales. These scales are associated with the development of complex convective patterns. These results confirm that an increase in Ra significantly increases the efficiency of convective heat transfer.

The effect of the Darcy number on the fluid flow and thermal fields for the fixed parameters is presented in Fig. 5 ($Ra = 10^5$, $\varepsilon = 0.8$, $l_x = 0.4$, $l_y = 0.2$). Isotherms and streamlines for different values of Da demonstrate that this parameter is a key governing factor of the convective flow inside the considered thermal system.

At $Da = 10^{-4}$ (Fig. 6a), the porous layer has minimal permeability and effectively functions as a barrier to liquid penetration. Convective circulation is maintained in air cavities with two symmetrical cells rotating in opposite directions. Isotherms within the porous region maintain a nearly vertical orientation. Heat transfer through the porous matrix occurs primarily due to the thermal conductivity of the solid skeleton. At $Da = 10^{-3}$ (Fig. 5b), permeability increases, and the ability of liquid to penetrate into the porous structure increases. The flow line demonstrates the expansion of the circulation cells into a porous region with a rise in the kinetic energy of the fluid flow. Convective cells exhibit a wider spatial extent and enhanced interaction at the liquid-porous interface. The isotherms exhibit moderate curvature within the porous layer. At $Da = 10^{-2}$ (Fig. 5*c*), the maximum permeability ensures significant convective penetration throughout the porous medium. The convective flow changes the structure: the circulation cells merge into a single dominant convective structure throughout the cavity. The isotherms exhibit pronounced distortion in both the liquid and porous regions. This mode demonstrates strong convective mixing inside the porous layer. Heat transfer increases significantly. At the same time, the efficiency of thermal insulation decreases.

Fig. 6 presents the effect of varying the Darcy number on the integral parameters ($Ra = 10^5$, $\varepsilon = 0.8$, $l_x = 0.4$, $l_y = 0.2$). The obtained results are consistent with the flow patterns shown in Fig. 6. Fig. 6a illustrates the temporal evolution of the maximum absolute value of the stream function for three Darcy numbers. The minimum values of flow intensity in the cavity are observed at $Da = 10^{-4}$, where the maximum stream function exhibits gradual monotonic growth with a steady-state value of $|\psi|_{\max} \approx 0.016$ after $\tau \approx 2000$. The prolonged transient phase reflects the slow development of convective structures when fluid penetration into the porous foam concrete medium is severely restricted by low permeability. At this Darcy number the high flow resistance imposed by the porous skeleton substantially inhibits fluid motion.

At intermediate permeability $Da = 10^{-3}$ the steady-state value is achieved later ($\tau \approx 2100$) with $|\psi|_{\max}$ stabilizing near 0.0035. Increased permeability allows for more intensive liquid penetration into the porous matrix and promotes a stronger connection between convective movement in the air spaces and the flow within the porous layer of foam concrete. This leads to the more rapid formation of circulation patterns and the rapid achievement of equilibrium.

At maximum permeability $Da = 10^{-2}$ the system reaches steady state by $\tau \approx 2500$ with $|\psi|_{\max} \approx 0.07$. This behavior confirms that increased permeability not only intensifies convective circulation but also accelerates the approach to thermal and hydrodynamic equilibrium. At high Da values the porous medium offers minimal resistance to fluid flow. Convective motion can be developed throughout the entire domain with minimal impediment from the solid foam concrete skeleton. The clear transition from a conductivity-dominated regime at low Da values ($Da = 10^{-4}$) to a convection-enhanced regime as Da increases to 10^{-2} demonstrates the progressive shift in the controlling heat transfer mechanism.

Fig. 6b presents the time-dependent evolution of the average Nusselt number at the hot wall for the three Darcy numbers. The average Nusselt number exhibits minimal changes across the entire range of Darcy numbers investigated. At $Da = 10^{-4}$ $\overline{Nu}$ stabilizes at approximately 2.0 after $\tau \approx 1700$. For $Da = 10^{-3}$ $\overline{Nu}$ reaches approximately 2.7 by $\tau \approx 2000$ while at $Da = 10^{-2}$ the steady-state value is approximately 4.5 achieved by $\tau \approx 3000$. The maximum change in the Nusselt number when the Darcy number is changed by three orders of magnitude is small compared to an increase in $|\psi|_{\max}$ over the same parameter range. Such behavior demonstrates that for a cavity with a porous foam concrete medium at $Ra = 10^5$ the total heat transfer is determined primarily by the thermal conductivity of the porous matrix (not by convective transfer).

The results demonstrate that increasing the permeability of the porous foam concrete layer can significantly improve air circulation and reduce moisture accumulation (through enhanced ventilation) without proportionally degrading thermal resistance. This suggests that moderately permeable porous insulation materials with relatively high thermal conductivity can maintain excellent thermal performance even under

conditions of intense internal convection. From a practical standpoint, this finding implies that foam concrete blocks with controlled porosity and permeability can be engineered to provide both good thermal insulation and adequate breathability, avoiding the common trade-off between these two properties. The weak sensitivity of Nusselt number to Darcy number variations also indicates that manufacturing tolerances in permeability control are less critical than might be expected, providing greater flexibility in the production process of insulation materials.

The influence of the porosity ε of the porous structure on the fluid flow rate and the average Nusselt number is presented in Fig. 7 ($Ra = 10^5$, $Da = 10^{-4}$, $l_x = 0.4$, $l_y = 0.2$). Fig. 7a presents the time-dependent evolution of $|\psi|_{\max}$ for four porosity values. At $\varepsilon = 0.1$ (low porosity configuration with a dense solid skeleton) the maximum stream function reaches approximately $|\psi|_{\max} \approx 0.03$ at steady state. This relatively high value indicates that the limited pore space does not significantly impede convective circulation within the air cavities. At this porosity the effective thermal conductivity of the porous layer is $\lambda_{\mathrm{pm}} = 0.9 \times 0.13 + 0.1 \times 0.022 \approx 0.119$ W/(m·K) which is nearly an order of magnitude higher than that of air. As porosity increases to $\varepsilon = 0.4$ $|\psi|_{\max}$ decreases to approximately 0.022 with the effective thermal conductivity reducing to $\lambda_{\mathrm{pm}} \approx 0.087$ W/(m·K). At $\varepsilon = 0.6$ the steady state value further decreases to approximately 0.018 while λ_{pm} reduces to approximately 0.065 W/(m·K). Finally, at $\varepsilon = 0.8$ (high porosity of the porous medium) the maximum stream function reaches its minimum value of $|\psi|_{\max} \approx 0.014$ with λ_{pm} decreasing to approximately 0.044 W/(m·K).

This monotonic decrease in circulation intensity with increasing porosity can be attributed to the competing thermal and hydrodynamic mechanisms associated with the properties of foam concrete and air. First, as porosity increases, the effective thermal conductivity of the porous region decreases according to $\lambda_{pm} = \varepsilon \cdot \lambda_f + (1-\varepsilon) \cdot \lambda_s$. Since $\lambda_s/\lambda_f \approx 5.9$ higher porosity significantly reduces λ_{pm}, decreasing from 0.119 W/(m·K) at $\varepsilon = 0.1$ to 0.044 W/(m·K) at $\varepsilon = 0.8$ a reduction of approximately 63%. However, this reduction in λ_{pm} paradoxically weakens convection because it diminishes the thermal coupling between the heated wall and the air cavities, reducing the temperature gradient that drives buoyancy forces in the fluid regions. Second, the effective heat capacity ratio $\eta = \varepsilon + (1-\varepsilon)\left((\rho c)_s / (\rho c)_f\right)$ decreases from approximately 392 at $\varepsilon = 0.1$ to 196 at $\varepsilon = 0.4$, 131 at $\varepsilon = 0.6$ and 79 at $\varepsilon = 0.8$, indicating that lower porosity configurations possess significantly higher thermal inertia. This greater thermal mass dampens transient temperature fluctuations but also modifies the thermal response of the system. Third, although permeability increases with porosity, at the fixed $Da = 10^{-4}$ considered here, the redistribution of foam concrete material alters the spatial distribution of thermal resistance. At low porosity, the dense porous skeleton near the heated wall conducts heat efficiently toward the air cavities, maintaining strong thermal gradients that sustain vigorous convection. At high porosity, the reduced solid fraction weakens this conductive pathway, diminishing the thermal driving force for convective circulation despite the lower flow resistance. The progressive decrease in $|\psi|_{\max}$ across the four porosity values demonstrates a consistent trend of convective suppression with increasing ε.

Fig. 7b demonstrates the corresponding time effect on the average Nusselt number for four porosity values. At $\varepsilon = 0.1$ the steady state value for the average Nusselt number ($\overline{Nu}$) reaches 1.2 indicating efficient convective heat transfer facilitated by the strong conductive coupling through the dense foam concrete skeleton. As porosity increases to $\varepsilon = 0.4$ the Nusselt number decreases to 1.1 reflecting the beginning of convective weakening. For $\varepsilon = 0.6$ Nusselt number further diminishes to approximately 1.0. Finally, at $\varepsilon = 0.8$ the Nusselt number reaches its minimum value of approximately 0.9. This systematic reduction in Nusselt number reflects the weakening of convective circulation shown in Fig. 7a, combined with the decreased effective thermal conductivity of the porous medium. The total decrease in $\overline{Nu}$ across the porosity range is considerably less pronounced than the corresponding reduction in $|\psi|_{\max}$. This disparity suggests that the

reduction in λ_{pm} with increasing porosity partially compensates for the diminished convective contribution by increasing the thermal resistance of the porous layer itself. The overall thermal insulation performance is improved due to the reduced conductive heat flux through the foam concrete matrix.

The combined influence of Ra and the size of the air cavities (l_x, l_y) on the fluid flow rate and $\overline{Nu}$ at $Da = 10^{-4}$, $\varepsilon = 0.8$ is presented in Fig. 8. According to Fig. 8a, variations in the air cavity geometry have a pronounced effect on the intensity of buoyancy-driven circulation. An increase in the cavity dimensions generally leads to higher values of the maximum stream function, indicating enhanced convective motion within the air gaps. Larger cavities reduce geometric confinement and promote the formation of more developed circulation structures, which is reflected in both increased flow intensity and extended transient behavior. In contrast, reduced cavity sizes suppress the development of convective cells, resulting in weaker circulation and faster attainment of steady-state conditions. The influence of cavity geometry becomes more evident with increasing Rayleigh number, highlighting the coupled role of buoyancy forces and spatial confinement.

Fig. 8b shows that the mean Nusselt number increases with increasing cavity dimensions, indicating an intensification of convective heat transfer at the heated boundary. However, the growth of the Nusselt number remains moderate compared to the corresponding increase in flow intensity. The overall heat transfer is still largely controlled by thermal conduction through the porous matrix. The low permeability of the porous layer effectively restricts the convective heat transport, maintaining a conduction-dominated regime across the investigated range of cavity sizes.

5 Conclusions

Thermogravitational convection within a closed rectangular porous domain in the presence of two air parts has been studied using non-primitive variables ψ (stream function) and ω (vorticity) with the help of the FDM. The comprehensive parametric analysis for $Ra = 10^4$–10^6, $Da = 10^{-4}$–10^{-2}, $\varepsilon = 0.1$–0.8, and varying air cavity geometries has been conducted.

The results indicate that increasing the Rayleigh number leads to a strong intensification of buoyancy-driven circulation, with the maximum absolute value of the stream function increasing by more than an order of magnitude as Ra rises from 10^4 to 10^6. Over the same range of Ra, the mean Nusselt number at the hot wall increases. In contrast, variations in the Darcy number over two orders of magnitude result in an increase in flow intensity, while the corresponding change in the mean Nusselt number does not exceed 6%. This demonstrates that heat transfer is primarily governed by thermal conduction through the porous matrix rather than by convective transport. Increasing porosity from $\varepsilon = 0.1$ to $\varepsilon = 0.8$ reduces the maximum stream function and decreases the mean Nusselt number. It demonstrates improving thermal insulation performance at higher porosity levels.

The analysis of air cavity geometry shows that enlarging the cavity dimensions leads to a noticeable increase in flow intensity but only a moderate increase in heat transfer. For the investigated configurations, the most favorable thermal insulation performance is achieved for relatively small cavity dimensions combined with high porosity ($\varepsilon \geq 0.6$) and low permeability ($Da \leq 10^{-4}$). In this case, convective motion is effectively suppressed, and heat transfer remains conduction-dominated. This configuration minimizes the mean Nusselt number while maintaining stable flow conditions. The obtained results provide quantitative guidelines for the design of energy-efficient building insulation systems based on porous materials with embedded air cavities.

In summary, the combined effects of cavity geometry, porous medium properties, and convective suppression provide a solid theoretical basis for the design of energy-efficient building insulation systems.

The results indicate that porous materials with controlled permeability and porosity can effectively balance thermal insulation performance and internal airflow regulation, operating predominantly in a conduction-dominated regime.

For practical building insulation applications, our results suggest the following design guidelines:

- hollow blocks should employ high porosity foam concrete ($\varepsilon \geq 0.6$) with low permeability ($Da \leq 10^{-4}$) to minimize convective heat transfer;
- air cavity dimensions should be minimized to suppress convection while maintaining the cavity geometry;
- In typical building envelope applications with moderate temperature fluctuations ($\Delta T \approx 20°C$–$30°C$), the system operates in a conductivity-dominant mode. Consequently, the material's thermal conductivity becomes the primary design parameter.

Acknowledgement: Not applicable.

Funding Statement: This work was supported by the Russian Science Foundation (Project No. 25-79-10293).

Author Contributions: The authors confirm contribution to the paper as follows: Conceptualization, Mikhail Sheremet and Igor Miroshnichenko; methodology, Mikhail Sheremet and Igor Miroshnichenko; software, Marina Astanina and Gennadii Shashkin; validation, Marina Astanina and Gennadii Shashkin; formal analysis, Marina Astanina; investigation, Marina Astanina; resources, Igor Miroshnichenko; data curation, Gennadii Shashkin; writing—original draft preparation, Marina Astanina and Gennadii Shashkin; writing—review and editing, Igor Miroshnichenko and Mikhail Sheremet; visualization, Marina Astanina; supervision, Mikhail Sheremet; project administration, Igor Miroshnichenko; funding acquisition, Igor Miroshnichenko. All authors reviewed and approved the final version of the manuscript.

Availability of Data and Materials: The data that support the findings of this study are available from the corresponding author, Igor Miroshnichenko, upon reasonable request.

Ethics Approval: Not applicable.

Conflicts of Interest: The authors declare no conflicts of interest.

Nomenclature

c	Thermal capacity, J/kg·K
Da	Darcy number
G	The gravitational constant, m/s^2
K	Porous layer's permeability, m^2
L	Size of the system in y-direction, m
L_1	Size of the system in x-direction, m
l_1	Dimensional size of the clear part in y-direction, m
l_2	Dimensional size of the clear part in x-direction, m
$l_y = l_1/L$	Dimensionless size of the clear part in y-direction
$l_x = l_2/L_1$	Dimensionless size of the clear part in x-direction
p	Static pressure, Pa
Nu	Nusselt parameter
$\overline{Nu}$	Average Nusselt parameter
Pr	Prandtl parameter
Ra	Rayleigh parameter
T	Temperature, K

T_c	Cold temperature, K
T_h	Hot temperature, K
t	Physical time, s
$\overline{u}, \overline{v}$	Physical velocity components in x- and y-direction, m/s
u, v	Scaled velocity components in x- and y-direction
$\overline{x}, \overline{y}$	Physical coordinates, m
x,y	Scaled coordinates

Greek symbols

$\alpha = \lambda/(\rho c)$	Thermal diffusivity, W/m^2·K
β	Coefficient of thermal expansion, 1/K
ΔT	Temperature drop, K
ε	Porosity
η	Ratio of the heat capacities
θ	Scaled temperature
λ	Thermal conductivity, W/m·K
μ	Dynamic viscosity, Pa·s
ν	Kinematic viscosity, m^2/s
ρ	Density, kg/m^3
τ	Scaled time
$\overline{\psi}$	Physical stream function, m^2/s
ψ	Scaled stream function
$\overline{\omega}$	Physical vorticity vector, 1/s
ω	Scaled vorticity vector

Subscripts

c	Cooling temperature of the side wall
f	Fluid
h	Heating temperature of the side wall
pT	Porous medium
s	Solid matrix

References

1. Hulle TB, Krishnaraj R, Ramanan MV, Nagaprasad N. Darcy number effects on natural convection around a porous cylinder in L-shaped enclosure using Lattice Boltzmann method. Sci Rep. 2025;15:8448. doi:10.1038/s41598-025-88548-6.
2. Jalili B, Emad M, Malekshah EH, Jalili P, Akgul A, Hassani MK. Investigating double-diffusive natural convection in a sloped dual-layered homogenous porous-fluid square cavity. Sci Rep. 2024;14:7393. doi:10.1038/s41598-024-57395-2.
3. Ajibade AO, Gambo JJ, Jha BK. Effects of darcy and viscous dissipation on natural convection flow in a vertical tube partially filled with porous material under convective boundary condition. Int J Appl Comput Math. 2024;10(2):84. doi:10.1007/s40819-023-01623-2.
4. Patrulescu FO, Grosan T, Cimpean DS. Significance of inclination and energy loss for a free convection flow in a chamber filled with a bidisperse porous medium. Transp Porous Media. 2025;152(11):91. doi:10.1007/s11242-025-02225-w.
5. Rahman MM, Saghir MZ, Vajravelu K, Pop I. Free convective heat transfer flow in a glass bead porous medium varying permeability and sinusoidal wall temperature. J Therm Anal Calorim. 2025;150:551–72. doi:10.1007/s10973-024-13535-4.

6. Shoaib Q, Mukherjee V, Marmaridou V, Sereda A, Satarawala PN, Carrillo JG, et al. Development and evaluation of sustainable henequen fibre foams for thermal insulation. Mater Today Sustain. 2025;31:101111. doi:10.1016/j.mtsust.2025.101111.
7. Ling HM, Yew MC, Yew MK, Saw LH. Analyzing recent active and passive cool roofing technology in buildings, including challenges and optimization approaches. J Build Eng. 2024;89:109326. doi:10.1016/j.jobe.2024.109326.
8. Yang J, Wang Y, Zhang X, Pan Y. Effect of Rayleigh numbers on natural convection and heat transfer with thermal radiation in a cavity partially filled with porous medium. Procedia Eng. 2015;121:1171–8. doi:10.1016/j.proeng.2015.09.131.
9. Oropeza-Perez I, Ostergaard PA. Active and passive cooling methods for dwellings: a review. Renew Sustain Energy Rev. 2018;82:531–44. doi:10.1016/j.rser.2017.09.059.
10. Ma D, Zhang S, Geng B, Jiang B, Yan T, Wang W, et al. Design and performance optimization of thermochemical energy storage reactor integrated high-thermal-conductivity porous structures. Appl Therm Eng. 2025;278:127265. doi:10.1016/j.applthermaleng.2025.127265.
11. Ngninjio VDN, Beyer C, Wang B, Bauer S. Experimental and numerical investigation of thermally induced convection along a high-temperature borehole heat exchanger. Appl Therm Eng. 2024;236:121345. doi:10.1016/j.applthermaleng.2023.121345.
12. Abdelbaki A, Zrikem Z. Simulation num rique des transferts thermiques couples a travers les parois alvolaires des batiments. Int J Therm Sci. 1999;38:719–30.
13. Abdelbaki A, Zrikem Z, Haghighat F. Identification of empirical transfer function coefficients for a hollow tile based on detailed models of coupled heat transfers. Build Environ. 2001;36:139–48 doi:10.1016/s0360-1323(99)00061-x.
14. Ait-taleb T, Abdelbaki A, Zrikem Z. Numerical simulation of coupled heat transfers by conduction, natural convection and radiation in hollow structures heated from below or above. Int J Therm Sci. 2008;47:378–87. doi:10.1016/j.ijthermalsci.2007.01.035.
15. Ait-Taleb T, Abdelbaki A, Zrikem Z. Transfer function coefficients for time varying coupled heat transfers in vertically heated hollow concrete bricks. Build Simul. 2008;1:303–10. doi:10.1007/s12273-008-8131-y.
16. Chihab Y, Essaleh L, Bouferra R, Bouchehma A. Numerical study for energy performance optimization of hollow concrete blocks for roofing in a hot climate of Morocco. Energy Convers Manage X. 2021;12:100113. doi:10.1016/j.ecmx.2021.100113.
17. Sun J, Fang L, Han J. Optimization of concrete hollow brick using hybrid genetic algorithm combining with artificial neural networks. Int J Heat Mass Transf. 2010;53:5509–18. doi:10.1016/j.ijheatmasstransfer.2010.07.006.
18. Khanafer K, Vafai K. Effect of a circular cylinder and flexible wall on natural convective heat transfer characteristics in a cavity filled with a porous medium. Appl Therm Eng. 2020;181:115989. doi:10.1016/j.applthermaleng.2020.115989.
19. Alam P, Madanan U. Thermal transport in porous media: effect of grain size in Darcy-Benard systems at high Rayleigh numbers. Int J Therm Sci. 2026;220:110409. doi:10.1016/j.ijthermalsci.2025.110409.
20. Paing ST, Anderson TN. Characterising the effects of geometry on the natural convection heat transfer in closed even-span gable-roof greenhouses. Therm Sci Eng Prog. 2024;48:102408. doi:10.1016/j.tsep.2024.102408.
21. Nada SA, Said MA. Effects of fins geometries, arrangements, dimensions and numbers on natural convection heat transfer characteristics in finned-horizontal annulus. Int J Therm Sci. 2019;137:121–37. doi:10.1016/j.ijthermalsci.2018.11.026.
22. Zhou C, Li J, Yan D, Zhao B, Zhou L. Experimental and numerical study on the effective thermal conductivity of carbon fibrous media for high temperature thermal insulation applications. Aerosp Sci Technol. 2025;166:110591. doi:10.1016/j.ast.2025.110591.
23. Volschenk G, O'Shea M, Shaughnessy B. A novel approach to thermal insulation modelling in soft and medium vacuum insulation systems. Cryogenics. 2024;144:103946. doi:10.1016/j.cryogenics.2024.103946.
24. Ullah S, Saddiq G, Majeed AH, Alazman I. Conjugated heat transfer of entropy generation and hybrid nanoparticles in a cavity. Int J Numer Methods Heat Fluid Flow. 2025;35(11):4224–47. doi:10.1108/HFF-04-2025-0229.

25. Jia H, Feng X, Cui B, Liu Z. Design and thermal insulation simulation of nano-SiO_2 foam concrete and vacuum insulation panel system for building exterior wall insulation. Energy. 2025;330:136833. doi:10.1016/j.energy.2025.136833.
26. Xuan Z-H, Fang W-Z, Lu Y-H, Yang C, Tao W-Q. Significance of the natural convection to the heat transfer of porous media: a pore-scale study. Int J Heat Mass Transf. 2024;222:125163. doi:10.1016/j.ijheatmasstransfer.2023.125163.
27. Mirzaei AM, Mehmandoosti MM, Bijarchi MA, Ganji DD. Investigation of entropy generation and natural convection in a trapezoidal porous enclosure with a square hole: a finite element analysis. Case Stud Therm Eng. 2025;70:106069. doi:10.1016/j.csite.2025.106069.
28. Ataei-Dadavi I, Chakkingal M, Kenjeres S, Kleijn CR, Tummers MJ. Flow and heat transfer measurements in natural convection in coarse-grained porous media. Int J Heat Mass Transf. 2019;130:575–84. doi:10.1016/j.ijheatmasstransfer.2018.10.118.
29. Taghavi M, Sharma S, Balakotaiah V. Natural convection effects in insulation layers of spherical cryogenic storage tanks. Int J Heat Mass Transf. 2024;220:124918. doi:10.1016/j.ijheatmasstransfer.2023.124918.
30. Veit M, Johra H, Rask N, Roesgaard SM, Jensen RL. Experimental investigations of internal macro-scale convection in the loose-fill wood fiber insulation layer of a full-scale wall element. Energy Build. 2026;350:116646. doi:10.1016/j.enbuild.2025.116646.
31. Angelotti A, Alongi A, Augello A, Dama A, De Antonellis S, Ravida A, et al. Thermal conductivity assessment of cotton fibers from apparel recycling for building insulation. Energy Build. 2024;324:114866. doi:10.1016/j.enbuild.2024.114866.
32. Yu YQ, Bergeron A, Licht JR. Numerical simulation of involute-plate research reactor flow behavior using RANS, LES and DNS. Ann Nucl Energy. 2024;207:110709. doi:10.1016/j.anucene.2024.110709.
33. Chen H-T, Lin M-C, Chang J-R. Numerical and experimental studies of natural convection in a heated cavity with a horizontal fin on a hot sidewall. Int J Heat Mass Transf. 2018;124:1217–29. doi:10.1016/j.ijheatmasstransfer.2018.04.046.
34. Aleshkova IA, Sheremet MA. Unsteady conjugate natural convection in a square enclosure filled with a porous medium. Int J Heat Mass Transf. 2010;53:5308–320. doi:10.1016/j.ijheatmasstransfer.2010.07.025.
35. Astanina MS, Sheremet MA. Numerical study of natural convection of fluid with temperature-dependent viscosity inside a porous cube under non-uniform heating using local thermal non-equilibrium approach. Int J Thermofluids. 2023;17:100266. doi:10.1016/j.ijft.2022.100266.
36. Nield DA, Bejan A. Convection in porous media. 3rd ed. New York, NY, USA: Springer Science + Business Media; 2006. 654 p.
37. Singh AK, Thorpe GR. Natural convection in a confined fluid overlying a porous layer—a comparison study of different models. Indian J Pure Appl Math. 1995;26:81–95 doi:10.1115/1.2910733.